



# Performance evaluation of thin active-edge planar sensors for the CLIC vertex detector<sup>☆</sup>



N. Alipour Tehrani<sup>a</sup>, M. Benoit<sup>b</sup>, D. Dannheim<sup>a</sup>, A. Fiergolski<sup>a</sup>, D. Hynds<sup>a,1</sup>, W. Klempt<sup>a</sup>,  
A. Macchiolo<sup>c,2</sup>, M. Munker<sup>a</sup>, A. Nürnberg<sup>a,\*</sup>

<sup>a</sup> CERN, Switzerland

<sup>b</sup> University of Geneva, Switzerland

<sup>c</sup> Max-Planck-Institut für Physik, Munich, Germany

## ARTICLE INFO

### Keywords:

Hybrid pixel detector  
Active edge  
Test-beam  
TCAD  
Timepix3  
CLIC

## ABSTRACT

Thin planar silicon sensors with a pitch of 55  $\mu\text{m}$ , active edge and various guard-ring layouts are investigated, using two-dimensional finite-element T-CAD simulations. The simulation results have been compared to experimental data, and an overall good agreement is observed. It is demonstrated that the 50  $\mu\text{m}$  thick active-edge planar silicon sensors with floating guard-ring or without guard-ring can be operated fully efficiently up to the physical edge of the sensor. The simulation findings are used to identify suitable sensor designs for application in the high-precision vertex detector of the future CLIC linear  $e^+e^-$  collider.

## 1. Introduction

The physics aims at the future  $e^+e^-$  Compact Linear Collider (CLIC) pose challenging requirements on the vertex detector [1]. Among other hybrid planar silicon pixel detectors are under study. The strict limit on the material budget of only 0.2% radiation length  $X_0$  per detector layer limits the active silicon thickness to only 50  $\mu\text{m}$ . Active-edge sensors can help to reduce the material content of the detector, by avoiding overlaps between neighbouring sensor tiles and still providing a good coverage of the solid angle.

Thin active-edge sensors with square pixels of 55  $\mu\text{m}$  pitch have been designed, fabricated and characterised in laboratory and test-beam studies using Timepix3 [2] readout chips as test vehicle. Different edge termination and guard-ring schemes have been implemented. Besides the evaluation of the tracking performance, the main focus of the study has been on breakdown behaviour and charge collection efficiency in the edge region.

The detection efficiency of planar silicon pixel sensors with implanted and activated edges is strongly dependent on the electric field distribution in the edge region and hence on the interplay between pixel geometry, guard-ring grounding scheme and edge implant. Optimisation of the edge design, in particular of the guard-ring structure and the distance of the pixels to the trench around the sensor perimeter is therefore of utmost importance. Therefore, the study is complemented by finite-element T-CAD device simulations.

The paper is organised as follows. In Section 2 the sensor design and the experimental and simulation setups are presented. In Section 3 experimental breakdown characteristics, signal collection and detection efficiency in the edge region are compared to simulation for different edge layouts and sensor thicknesses. The findings are summarised in Section 4 and an outlook to further studies with smaller pixel size is given.

## 2. Active-edge sensors and simulation setup

In order to achieve full area coverage in the experiment, non-active regions have to be minimised. Active-edge processing is a technology aiming at eliminating the inactive silicon at the sensor edge, offering the possibility of seamlessly tiling individual sensors without the need for overlaps. Using a deep reactive ion-etching process, a trench at the sensor edge is formed. Ion implantation of the walls results in an extension of the backside electrode to the edge of the sensor [3]. Consequently the depletion zone is extended and the sensor is able to detect particles passing close to its physical edge. After the sensors are separated, the trench becomes the sensor edge and defines the physical size of the sensor. Using this technology n-in-p sensors matching the Timepix3 layout with a matrix size of 256  $\times$  256 pixels of 55  $\mu\text{m}$   $\times$  55  $\mu\text{m}$  size have been produced by Advacam [4]. Due to the extension of the backside contact to the edge, the potential gradient

<sup>☆</sup> This work was carried out in the framework of the CLICdp collaboration.

\* Correspondence to: KIT, Karlsruhe, Germany.

E-mail address: [andreas.nurnberg@cern.ch](mailto:andreas.nurnberg@cern.ch) (A. Nürnberg).

<sup>1</sup> Now at: NIKHEF, Amsterdam, The Netherlands.

<sup>2</sup> Now at: University of Zurich, Switzerland.

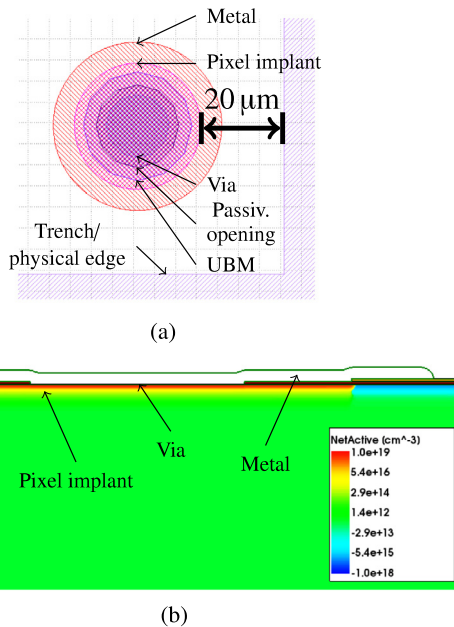


Fig. 1. Pixel and edge layout of the investigated sensor designs: (a) Top view of the layout of a sensor with 20 μm edge distance without guard-ring and (b) cross-section through the pixel layout as implemented in the two-dimensional simulation. The colour scale indicates the effective doping concentration (colour on-line).

Table 1

Summary of the investigated sensor layouts. Edge distance refers to the distance between the active edge and the last pixel implant.

Thickness	Bias voltage	Edge dist.	GR layout
50 μm	-15 V	20 μm	None
50 μm	-15 V	50 μm	None
50 μm	-15 V	23 μm	Floating
50 μm	-15 V	50 μm	Floating
50 μm	-15 V	28 μm	Grounded
50 μm	-15 V	55 μm	Grounded
100 μm	-20 V	55 μm	Grounded
150 μm	-30 V	55 μm	Grounded

between the outermost pixels (close to ground potential) and the sensor edge (bias voltage) makes this type of sensor prone to early breakdown. To smoothen the potential gradient, guard-rings are placed between the outermost pixel cell and the sensor edge, surrounding the full pixel matrix. These guard-rings can either be connected to ground potential through an additional row of grounded pixel pads on the Timepix3 chip or can be kept floating. A low dose p-spray implantation is applied to the front-side of the sensor in order to avoid shorts between pixels by electron accumulation at the interface between silicon bulk and oxide.

### 2.1. Device layout and simulated structures

Active-edge sensors with six different guard-ring layouts and three different thicknesses between 50 μm and 150 μm have been investigated. Fig. 1 depicts one of the edge layouts graphically and gives details on the implementation of the pixel in the simulation. Circular implants have been chosen to minimise the detector capacitance. No negative impact on the detector performance, like inefficient regions between pixels, were observed. Table 1 summarises important parameters of all tested devices, especially the edge distance, which is defined as the distance between the last pixel implant and the physical edge of the sensor.

Figs. 2 and 3 illustrate the simulated two-dimensional cross section through the sensor layout. Pixels in neighbouring columns, the optional guard-ring and the cut edge are simulated. The choice to simulate two

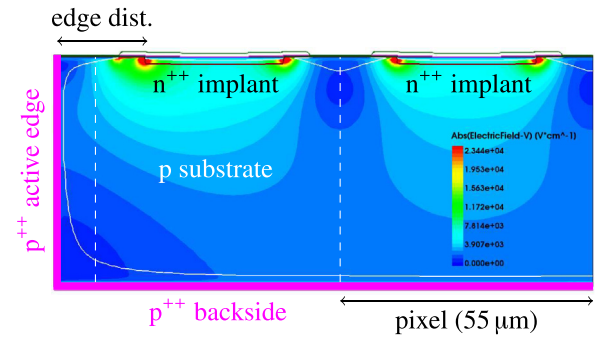


Fig. 2. Electric field distribution in a 50 μm thick planar sensor at -15 V bias voltage in the 2d cross section. The solid white line indicates the border of the depletion volume, the dashed white lines indicate the 55 μm pixel grid (colour on-line).

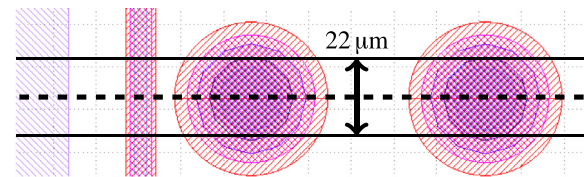


Fig. 3. Illustration of the simulated cross section through the sensor layout (dashed line) and geometrical restriction of the reconstructed tracks used for comparing the experimental results with the 2d-simulation (solid lines).

pixels next to the edge region is motivated by the comparison of the electric field distribution in a 150 μm thick device with two pixels to a device with four pixels, as shown in Fig. 4. Since the electric field is very similar close to the active edge, and only slight differences close to the boundary within the pixel matrix occur, the simulation has been limited to the active edge and two pixels. In thinner devices, the influence of the boundary condition on the electric field close to the edge is even smaller. The necessary computing time to perform a three-dimensional simulation of the device has been found to be several orders of magnitude higher than for the two dimensional case, even for static simulations. Simplifications of the geometry, e.g. simulating on a coarser mesh, would speed up the computation while simultaneously reduce the accuracy. For that reason a two-dimensional simulation has been chosen.

### 2.2. Experimental setup

Experimental studies on active-edge sensors have been performed using Timepix3 readout ASICs. The sensors have been operated as Device-Under-Test (DUT) in a Timepix3 reference telescope [5,6] in a 120 GeV pion beam at the SPS H6 beam line at CERN. The resolution of ~2 μm of the reconstructed track position on the DUT allows for a position dependent analysis of the charge collection properties close to the sensor edge. For better comparability of the two-dimensional simulation with the experimental results, only tracks reconstructed within ±11 μm around the centre of the pixel row are considered, as illustrated in Fig. 3 by the solid lines.

Current-Voltage (IV) characteristics have been recorded at room temperature using a source-meter. During these measurements, the ASICs were not powered, and thus the thermal load from the ASICs was not present. During operation, the sensors are expected to be warmer and the current to be higher.

### 2.3. T-CAD simulation setup

The simulations are performed using the finite-element T-CAD software Synopsys Sentaurus Device [7] in version I-2013.12. Both static

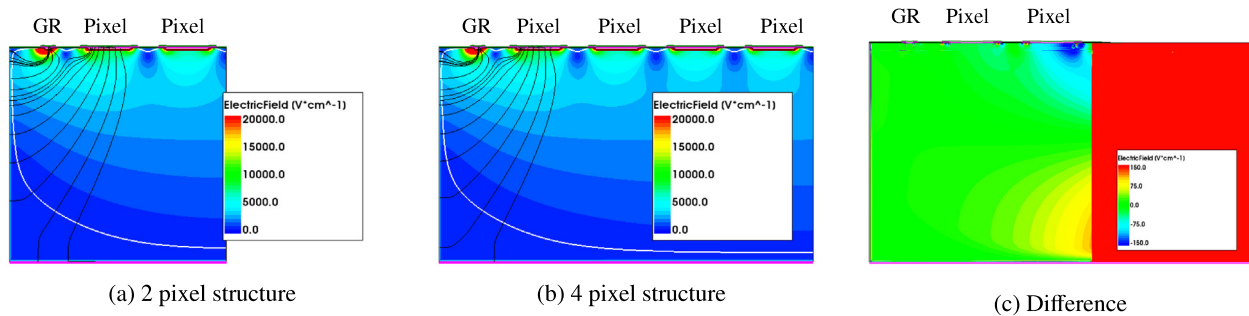


Fig. 4. Comparison of the electric field distribution in a 150  $\mu\text{m}$  thick active edge sensor with 55  $\mu\text{m}$  edge distance and grounded guard-ring at  $-30\text{ V}$  with (a) 2 and (b) 4 simulated pixels next to the edge, to investigate the influence of the applied boundary condition towards the regular pixel matrix on the electric field in the edge region. (c) shows the difference in the electric field between both cases (colour on-line).

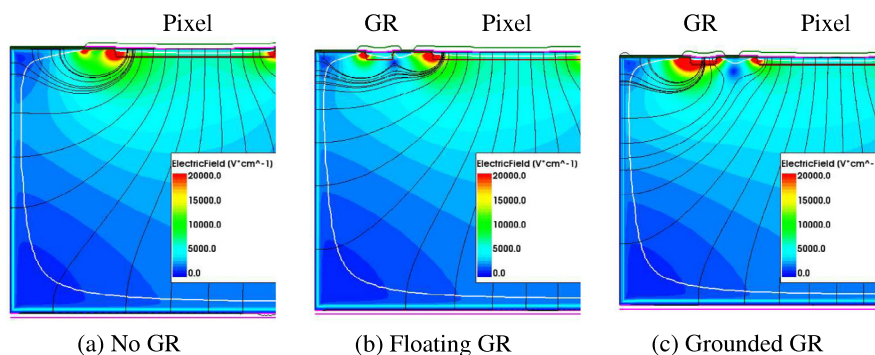


Fig. 5. Electric field distribution in 50  $\mu\text{m}$  thick sensors close to the edge for different guard-ring layouts at  $-15\text{ V}$  bias. The solid white line indicates the border of the depletion volume (colour on-line).

and transient simulations are performed. The device temperature has been set to 293 K, and the Van Overstraeten–De Man model [8] has been applied to include avalanche multiplication in the simulation and to extract the breakdown voltage of the device. At the device boundary, the components of the electric field and carrier currents perpendicular to the surface are set to zero. For contacts connected to external circuitry (backside, pixels and grounded guard-ring), the potential is fixed to the external voltage, while for floating contacts (floating guard-rings) a zero-current condition is applied. The density of the fixed charge at the Si–SiO<sub>2</sub> interface has been varied between  $1 \times 10^{10}\text{ cm}^{-2}$  and  $1 \times 10^{11}\text{ cm}^{-2}$ , and no significant impact on the device performance has been found. In the following, an fixed charge density of  $1 \times 10^{10}\text{ cm}^{-2}$  is used. After defining the geometry, the bias voltage on the backside contact is ramped to the nominal value in a quasi-static simulation. From that, the IV characteristics and the electric field distribution in the sensor can be extracted.

In a second step, a particle hit is simulated by introducing the ionisation charges using the heavy ion model. A given amount of e–h pairs is distributed in time and space, according to the linear energy transfer of the particle. 500 ps after the start of the time dependent simulation, charge carriers are created along the particle path with a Gaussian profile with width of 0.5  $\mu\text{m}$  and a linear energy transfer of 0.01 fC  $\mu\text{m}^{-1}$ , corresponding to about 62 e–h pairs/ $\mu\text{m}$ . The drift of these charges in the sensor volume is tracked in a time-dependent simulation. Simultaneously, the induced current on all electrodes is recorded. By integrating the current pulses over the simulation time, the total induced charge is extracted. In fully depleted thin sensors, the signal charge is collected within a few ns. For most of the simulations presented in the following, the simulation time has thus been set to 15 ns. To study slower processes like capacitive effects on the floating contacts, the simulation time has been extended to 20 ms.

### 3. Simulation results and comparison with experimental data

#### 3.1. Electric field

The electric field configuration close to the sensor edge depends on the guard-ring layout, as illustrated in Fig. 5. Without guard-ring and with floating guard-ring, the electric field extends directly from the sensor edge to the last pixel row. In devices with floating guard-ring, the high-field region between the last pixel and the active edge is reduced. In devices with grounded guard-ring, some field lines extend from the sensor edge to the guard-ring. This indicates that part of the ionisation charge is collected by the guard-ring and the charge collection efficiency of the last pixel will be reduced.

#### 3.2. IV characteristics and breakdown

Due to the extension of the backside electrode to the sensor edge, the electric field in the region between the edge implant and the pixel implant can be high. This makes the sensor prone to early breakdowns. To extract the breakdown voltage, the voltage on the backside electrode is increased above the nominal operation point until a steep increase of the reverse current is observed. Fig. 6 shows the measured IV characteristics of the full sensor for the investigated edge geometries, and Fig. 7 for two simulated pixels and the different simulated edge termination schemes for the 50  $\mu\text{m}$  thick sensors. Above a certain electric field strength, avalanche ionisation is releasing plenty of free charge carriers in the silicon bulk and thus the breakdown is closely linked to the distribution of the electric field.

In data, the devices without guard-ring and edge distance of 20  $\mu\text{m}$  and 50  $\mu\text{m}$  show a similar breakdown around 125 V, whereas in the device with floating guard-ring and edge distance of 50  $\mu\text{m}$ , the breakdown voltage is improved to about 180 V. In the device with floating guard-ring and narrow edge distance of 23  $\mu\text{m}$ , the breakdown appears already around 90 V.

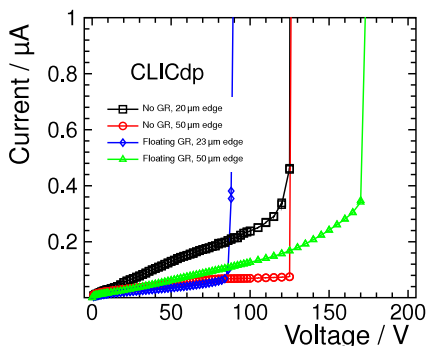


Fig. 6. Measured IV characteristics of the 50µm thick sensors with different investigated edge termination geometry.

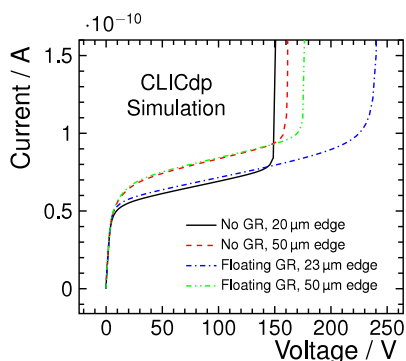


Fig. 7. Simulated IV characteristics of the 50µm thick sensors with different edge layouts.

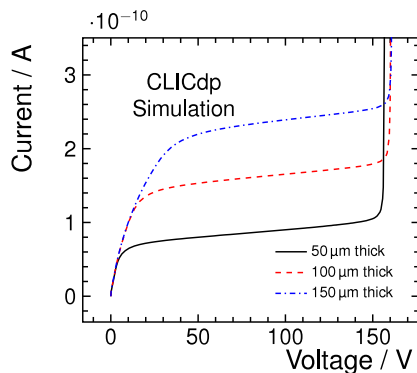


Fig. 8. Simulated IV characteristics of the 50µm, 100µm and 150µm thick active-edge sensors with grounded guard-ring and 55µm edge distance.

In the device simulations, both sensors without guard-ring show the breakdown of the junction around 150 V, with slightly higher breakdown voltage of the wider edge layout, similar to the experimental results. The addition of a floating guard-ring smoothens the voltage drop in the silicon bulk close to the surface and reduces the electric field strength at a given voltage, which results in a higher breakdown voltage. In contrast to the experimental result for the narrow edge layout, the breakdown voltage is significantly increased in the simulation, up to 240 V. The qualitatively different behaviour of the breakdown voltage for the narrow edge design with floating guard-ring hints at another source of the breakdown unrelated to the edge region in the measured device in that particular sensor.

The potential gradient between the edge implant and the guard-ring does not significantly depend on the sensor thickness, if the same edge

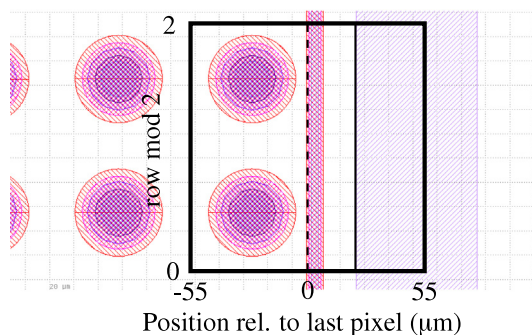


Fig. 9. Definition of the coordinate system for the in-pixel resolved efficiency studies: For all 256 pixel rows, the last pixel column and the edge region is considered.

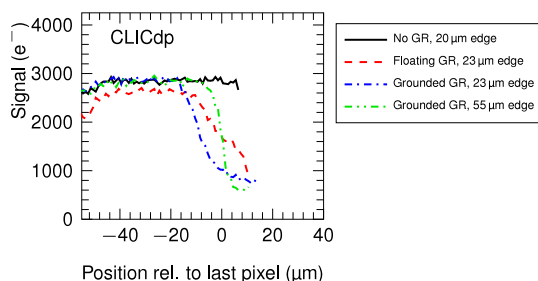


Fig. 10. Experimentally obtained most probable signal value for 50µm thick sensors with different edge layout. For the device with 55µm wide edge and grounded guard-ring, the signal drops below the detection threshold of  $\sim 600e^-$  applied in the experimental studies.

layout is implemented. For that reason, the simulated breakdown in the 50µm, 100µm and 150µm thick sensors with grounded guard-ring is appearing around 150 V for all thicknesses, as illustrated in Fig. 8.

### 3.3. Charge collection and efficiency in 50µm thick sensors

Exploiting the good pointing capabilities of the reference telescope, the collected signal and the hit efficiency of the active-edge region have been studied as a function of the track incident point. The efficiency has been mapped in two dimensions. For the last two columns, all 256 pixel rows are mapped to a  $2 \times 2$  pixel plot (see Fig. 9 for definition of the coordinates).

The experimentally measured charge collection close to the sensor edge is summarised in Figs. 10 and 11. As already illustrated in Fig. 3, for better comparability with the 2d-simulations, only particle tracks which pass the sensor within the central 40% of the pixel cell area are considered.

In devices without guard-ring, the recorded signal is constant up to the physical edge of the sensor, as the pixel implants are the only available contacts towards which the charges can drift. This is illustrated by the signal distribution as a function of the track incident position close to the sensor edge, shown in Figs. 10 and 11(a). In devices with floating guard-ring, a reduction of the signal for particles passing close to the edge with respect to the pixel matrix and to devices without guard-ring is observed, as shown in Figs. 10 and 11(b).

A significant loss of signal to grounded guard-rings is observed for tracks passing the sensor after the last pixel, as visible in Figs. 10, 11(c) and 11(d).

For a comparison of the collected charge, a simulated particle hit has been scanned along the sensor. For each position, the total charge recorded by both pixels is summed up. However in the simulation, no per-pixel threshold is applied to the charge signal, and Landau fluctuations of the signal deposition and delta electrons are not taken

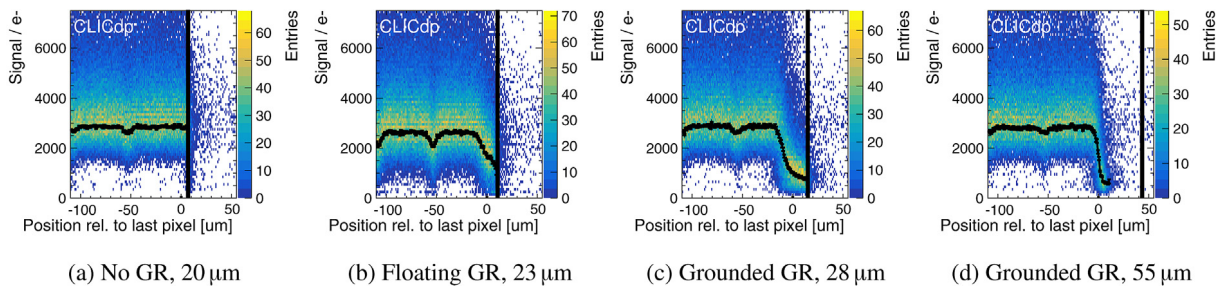


Fig. 11. Experimentally obtained signal distribution close to the sensor edge for 50 μm thick sensors with different edge layout. The vertical solid line indicates the physical edge of the sensor. The solid black line superimposed on the histogram indicates the most probable value of the cluster signal per x-bin (colour on-line).

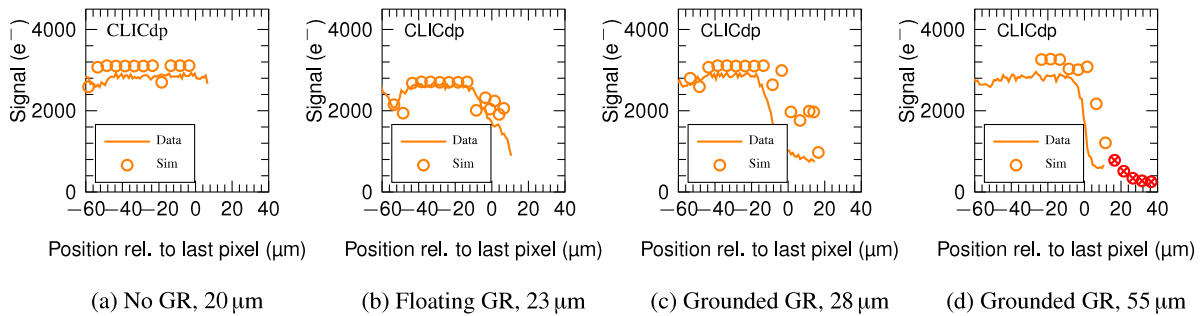


Fig. 12. Comparison of the simulated signal near the sensor edge to the experimentally obtained most probable signal value for 50 μm thick sensors with different edge layout (cf. Fig. 11). For the device with 55 μm wide edge and grounded guard-ring, the simulated signal drops below the detection threshold of ~600e<sup>-</sup> applied in the experimental studies. This is indicated by the style change in the simulated curve.

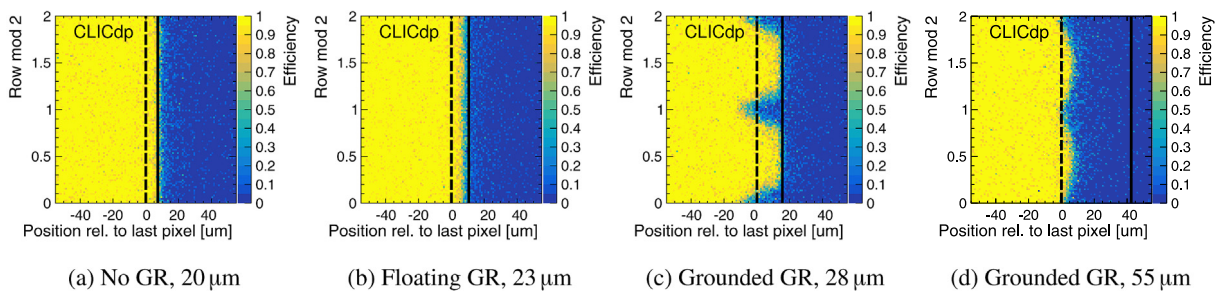


Fig. 13. Experimentally obtained detection efficiency close to the sensor edge for 50 μm thick sensors with different edge layout. The dashed vertical line indicates the end of the regular pixel structure, the solid line indicates the physical edge of the sensor (colour on-line).

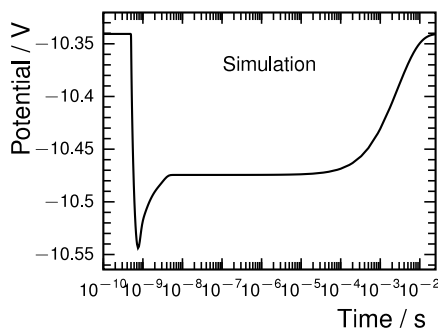


Fig. 14. Electric potential on a floating guard-ring after a particle hit close to the sensor edge, 500 ps after the start of the simulation. Relaxation to the equilibrium is achieved only after several ms. Due to the short peaking time of the Timepix3 ASIC of 30 ns, charge stored on the guard-ring (in this example about 330e<sup>-</sup>) is lost for detection.

simulation results are attributed to meshing effects close to the guard-ring structure. For the device without guard-ring, no signal drop at the sensor edge is observed, whereas the loss of signal to the floating guard-ring is reproduced by the simulation model. For the two grounded guard-ring options, a strong loss of signal is observed. In the wider edge configuration, the signal drops below the detection threshold of 600 to 1000 electrons, that has been set for the experimental studies, explaining the observed inefficiency of the device.

The signal drop in devices with floating guard-ring can be explained by the capacitive coupling of the guard-ring to the surrounding implants. Since the guard-ring is not kept at a fixed potential, charge can be collected by the implant in the non-equilibrium state after a particle hit. In this particular case, the stored charge given by the simulator is about  $5.4 \times 10^{-17}$  C or 330 e<sup>-</sup>. This additional charge on the guard-ring implant results in a shift of the electrostatic potential of the implant due to its capacitance to the surrounding contacts, as illustrated in Fig. 14 for a transient simulation of 20 ms. With time, the device returns to equilibrium, and the charge gets collected in the readout implants. The time needed to relax to the static state is longer than the 30 ns peaking time of the Timepix3 front-end, and thus charge stored on the guard-ring does not contribute to the signal. In the simplified two-dimensional simulation, this effect can only be studied qualitatively,

into account. The trends observed in the experimental data are reproduced by the simulation (see Fig. 12). The slight fluctuations on the

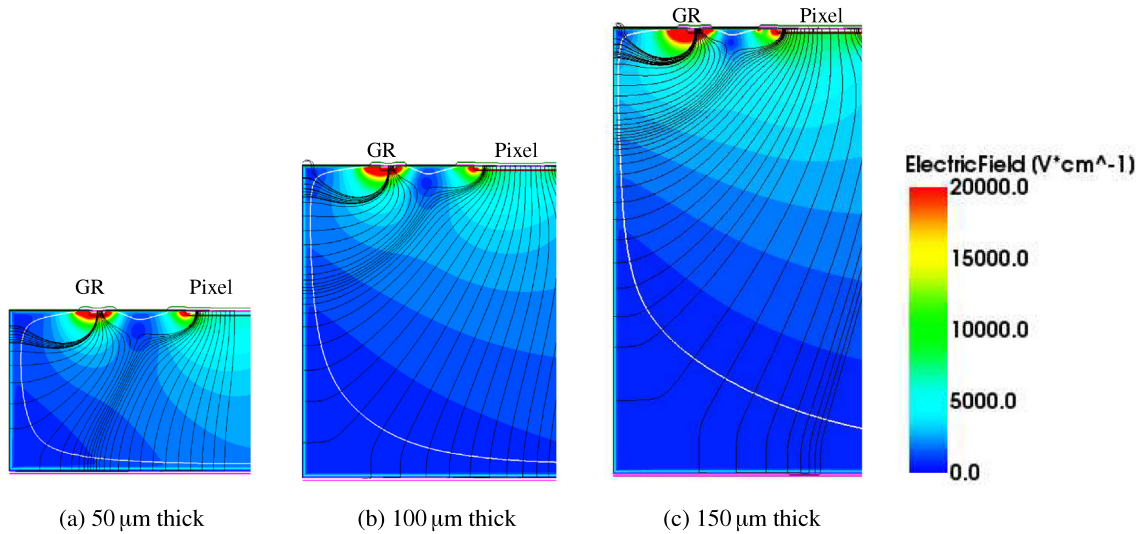


Fig. 15. Electric field distribution close to the sensor edge in (a) 50  $\mu\text{m}$  (operated at  $-15\text{ V}$ , full depletion at  $-7\text{ V}$ ), (b) 100  $\mu\text{m}$  (operated at  $-20\text{ V}$ , full depletion at  $-12\text{ V}$ ) and (c) 150  $\mu\text{m}$  (operated at  $-30\text{ V}$ , full depletion at  $-15\text{ V}$ ) thick active-edge sensors with grounded guard-ring and 55  $\mu\text{m}$  edge distance. The solid white line indicates the border of the depleted volume (colour on-line).

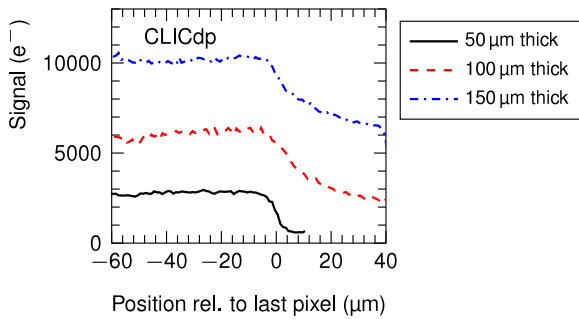


Fig. 16. Experimentally obtained most probable signal value for 50  $\mu\text{m}$ , 100  $\mu\text{m}$  and 150  $\mu\text{m}$  thick sensors with 55  $\mu\text{m}$  edge and grounded guard-ring. For the 50  $\mu\text{m}$  thick device, the signal drops below the detection threshold of  $\sim 600e^-$  applied in the experimental studies.

as the capacitance of the several centimetre long guard-ring is not modelled accurately.

As already deduced from the signal distributions in Fig. 11, the device without guard and the device with floating guard-ring are fully efficient up to the physical edge of the silicon, whereas for both sensors with grounded guard-ring a significant loss of efficiency can be observed, as shown in Fig. 13. This can be attributed to the fact that the grounded guard-ring and the last pixel implant are competing in collecting the ionisation charge. If the guard-ring is the closest implant to the particle hit, most of the signal is collected there and is lost for detection. This is especially the case between two pixel rows.

### 3.4. Dependence of the edge efficiency on the sensor thickness

The performance of the active-edge devices depends on the sensor thickness.

The simulated distributions of the electric field are shown in Fig. 15. In the edge region of the thicker device, only the field lines originating close to the sensor surface reach to the grounded guard-ring. From a significant sensor volume deeper in the bulk the field is pointing to the pixel electrode.

The signal and detection efficiency for the three different thicknesses is illustrated in Figs. 17–19. For thin sensors, the charge loss to grounded guard-rings can be significant and can lead to inefficient

operation of the sensor. The grounded guard-ring layout with 55  $\mu\text{m}$  edge distance has been investigated experimentally on 50  $\mu\text{m}$ , 100  $\mu\text{m}$  and 150  $\mu\text{m}$  thick sensors. As in the 50  $\mu\text{m}$  thick sensors, also in the thicker sensors a substantial charge loss to the guard-ring is observed. This is illustrated in Figs. 16 and 17, where the signal distribution close to the sensor edge for a 50  $\mu\text{m}$ , 100  $\mu\text{m}$  and 150  $\mu\text{m}$  thick sensor is compared.

The qualitative agreement between the simulated and the experimentally obtained signal distribution is shown in Fig. 18.

Due to the overall larger amount of ionisation charge in the thicker devices, the signal does not drop below the detection threshold. For that reason, particles passing the sensor close to its physical edge can still be detected efficiently. This is shown in the two-dimensional efficiency maps in Fig. 19.

The influence of the sensor thickness on the charge collection efficiency at the edge is further clarified by investigating the simulated electric field for the three different sensor thicknesses, illustrated in Fig. 15. In the 50  $\mu\text{m}$  thick device, most field lines reach from the edge directly to the grounded guard-ring. Therefore, most of the charge created in the edge is collected by the guard-ring and is lost for particle detection. In addition, the non-depleted volume near the sensor edge close to the backside adds to the charge loss. In the thicker devices, most field lines from the edge region deeper in the bulk reach the pixel implant, and thus charge deposited deeper in the sensor bulk is still collected by the first pixel. This enables the device to detect particles passing close to the sensor physical edge fully efficiently, while it also explains the observed signal loss to the guard-ring in the edge region of the thicker devices. Similar behaviour has been reported earlier for 200  $\mu\text{m}$  thick sensors [9].

## 4. Conclusions and outlook

Thin planar silicon sensors with active edge and various guard-ring layouts have been investigated using two-dimensional finite-element T-CAD simulations and with Timepix3 ASICs in test-beams. The detection efficiency as well as the charge collection efficiency strongly depend on the interplay between sensor thickness, guard-ring position and guard-ring connection scheme. The simulation results have been compared to experimental data, and an overall good agreement has been achieved. It has been demonstrated that 50  $\mu\text{m}$  thick active-edge planar silicon sensors with floating guard-ring or without guard-ring can be operated fully efficiently up to the physical edge of the sensor. To prevent

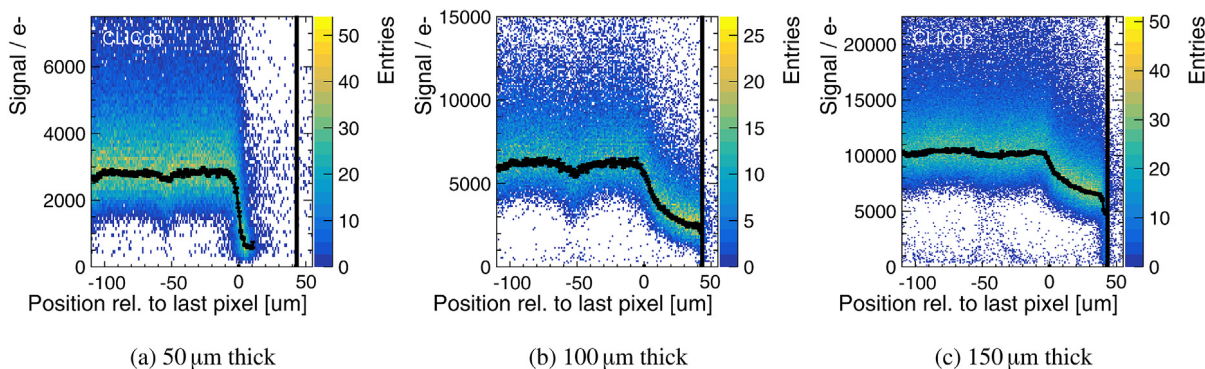


Fig. 17. Signal distribution close to the sensor edge for 50 μm, 100 μm and 150 μm thick sensors with grounded guard-ring and 55 μm edge distance. The vertical solid line indicates the physical edge of the sensor. The solid black line superimposed on the histogram indicates the most probable value of the cluster signal per x-bin (colour on-line).

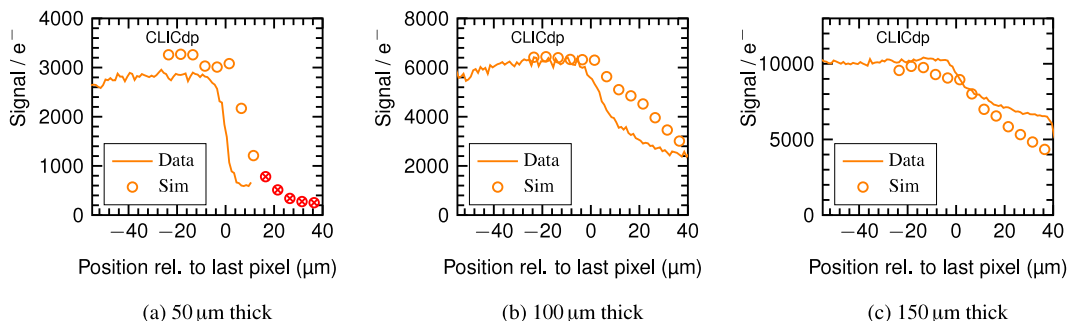


Fig. 18. Comparison of the simulated signal distribution close to the edge to the experimentally obtained results in 50 μm (at -15 V), 100 μm (at -20 V) and 150 μm (at -30 V) thick active-edge sensors with grounded guard-ring and 55 μm edge distance (cf. Fig. 17). For the 50 μm thick device, the simulated signal drops below the detection threshold of ~ 600e<sup>-</sup> applied in the experimental studies. This is indicated by the style change in the simulated curve.

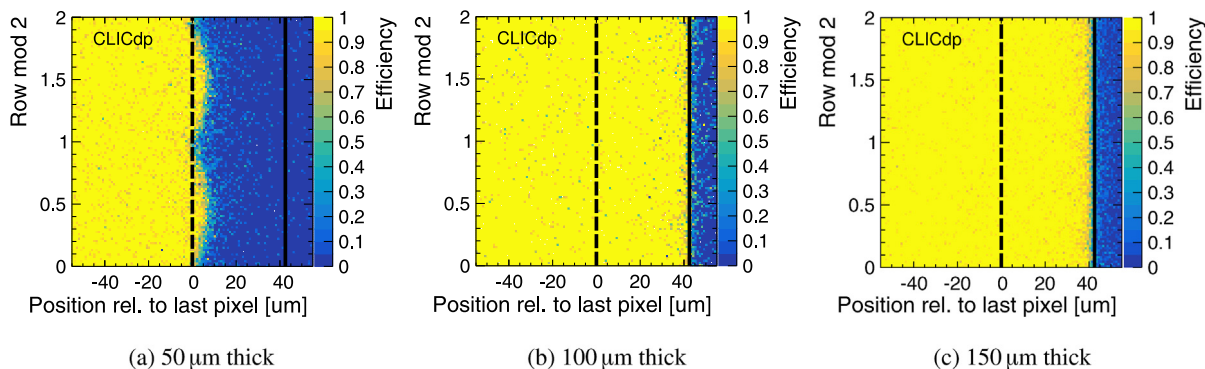


Fig. 19. Experimentally obtained efficiency map in 50 μm, 100 μm and 150 μm thick active-edge sensors with grounded guard-ring and 55 μm edge distance. The dashed vertical line indicates the end of the regular pixel structure, the solid line indicates the physical edge of the sensor (colour on-line).

early breakdowns, a floating guard-ring can be placed around the pixel matrix, without a significant impact on the detection efficiency. For application in the CLIC vertex detector, 50 μm thick sensors with narrow edge design and floating guard-ring as well as the design without guard-ring present a viable solution to achieve fully efficient particle detection up to the physical sensor edge with sufficient margin to the sensor breakdown. If necessary, further optimisation of the guard-ring distance to the pixel implants could be performed. Prototype sensors with a pixel size of 25 μm have been produced in a similar active-edge process and are currently under test in combination with CLICpix2 ASICs [10].

**Acknowledgements**

The authors thank Fernando Duarte Ramos (CERN) for his support with the mechanical integration of the tested devices in the telescope

system. The help from the staff operating the CERN SPS and the North Area test facilities is gratefully acknowledged. This project has received funding from the European Union’s Horizon 2020 Research and Innovation programme under Grant Agreement no. 654168. This work has been sponsored by the Wolfgang Gentner Programme of the German Federal Ministry of Education and Research, Germany.

**References**

[1] CLIC Conceptual Design Report: Physics and Detectors at CLIC, 2012, [arXiv:1202.5940](https://arxiv.org/abs/1202.5940).  
 [2] T. Poikela, J. Plosila, T. Westerlund, M. Campbell, M.D. Gaspari, X. Llopart, V. Gromov, R. Kluit, M. van Beuzekom, F. Zappone, V. Zivkovic, C. Brezina, K. Desch, Y. Fu, A. Kruth, Timepix3: a 65K channel hybrid pixel readout chip with simultaneous ToA/ToT and sparse readout, JINST 9 (05) (2014) C05013, [http://dx.doi.org/10.1088/1748-0221/9/05/C05013](https://doi.org/10.1088/1748-0221/9/05/C05013), <http://stacks.iop.org/1748-0221/9/i=05/a=C05013>.

- [3] X. Wu, et al., Recent advances in processing and characterization of edgeless detectors, JINST 7 (02) (2012) C02001, <http://dx.doi.org/10.1088/1748-0221/7/02/C02001>, <http://stacks.iop.org/1748-0221/7/i=02/a=C02001>.
- [4] Advacam Oy, Tietotie 3, 02150 Espoo, Finland, URL <http://www.advacam.com>.
- [5] N. Alipour Tehrani, Test-beam measurements and simulation studies of thin pixel sensors for the CLIC vertex detector (Ph.D. thesis), ETH Zurich, Diss. ETH No. 24216, CERN-THESIS-2016-311, 2017, <http://dx.doi.org/10.3929/ethz-b-000164813>.
- [6] S.E. Richards, The LHCb VELO upgrade, POS(VERTEX2015)008.
- [7] Synopsys, Inc., T-CAD, URL <https://www.synopsys.com/silicon/tcad.html>.
- [8] R.V. Overstraeten, H.D. Man, Measurement of the ionization rates in diffused silicon p-n junctions, Solid-State Electron. (ISSN: 0038-1101) 13 (5) (1970) 583–608, [http://dx.doi.org/10.1016/0038-1101\(70\)90139-5](http://dx.doi.org/10.1016/0038-1101(70)90139-5), <http://www.sciencedirect.com/science/article/pii/0038110170901395>.
- [9] M. Bomben, A. Ducourthial, A. Bagolini, M. Boscardin, L. Bosisio, G. Calderini, L. D'Eramo, G. Giacomini, G. Marchiori, N. Zorzi, A. Rummler, J. Weingarten, Performance of active edge pixel sensors, J. Instrum. 12 (05) (2017) P05006, <http://dx.doi.org/10.1088/1748-0221/12/05/p05006>.
- [10] E. Santin, P. Valerio, A. Fiergolski, CLICpix2 user's manual (EDMS 1800546 v.1), <https://edms.cern.ch/document/1800546/1>.